Mon. Not. R. Astron. Soc. **000**, 1–?? () Printed 9 March 2016 (MN LATEX style file v2.2)

# 3D-modelling of the stellar auroral radio emission

P. Leto[1] ⋆, C. Trigilio[1], C. S. Buemi[1], G. Umana[1], A. Ingallinera[1], L. Cerrigone[2]
[1]*INAF - Osservatorio Astrofisico di Catania, Via S. Sofia 78, 95123 Catania, Italy*
[2]*ASTRON, the Netherlands Institute for Radioastronomy, PO Box 2, 7990 AA Dwingeloo,The Netherlands*

arXiv:1603.02423v1 [astro-ph.SR] 8 Mar 2016

**ABSTRACT**
The electron cyclotron maser is the coherent emission process that gives rise to the radio lighthouse effect observed in the hot magnetic chemically peculiar star CU Virginis. It has also been proposed to explain the highly circularly polarized radio pulses observed on some ultra cool dwarfs, with spectral type earlier than M7. Such kind of coherent events resemble the auroral radio emission from the magnetized planets of the solar system. In this paper, we present a tridimensional model able to simulate the timing and profile of the pulses emitted by those stars characterized by a dipolar magnetic field by following the hypothesis of the laminar source model, used to explain the beaming of the terrestrial auroral kilometric radiation. This model proves to be a powerful tool to understand the auroral radio-emission phenomenon, allowing us to derive some general conclusions about the effects of the model's free parameters on the features of the coherent pulses, and to learn more about the detectability of such kind of pulsed radio emission.

**Key words:** masers – polarization – stars: chemically peculiar – stars: magnetic field

## 1 INTRODUCTION

The Electron Cyclotron Maser (ECM) is a coherent emission mechanism excited by the inverse velocity distribution that an electron population propagating along the converging field lines of a density-depleted magnetospheric cavity can develop. This mechanism (Wu & Lee 1979; Melrose & Dulk 1982) amplifies the extraordinary magneto-ionic mode, producing almost 100% circularly polarized radiation at frequency close to the local gyrofrequency ($\nu_B \propto B$). The maser amplification can occur within the magnetospheric region covering a wide range of magnetic field strength, providing observable ECM emission over a wide frequency range. The ECM is the mechanism responsible for the broad-band auroral radio emission from the magnetized planets of the solar system, such as the terrestrial auroral kilometric radiation (AKR), the Jupiter decametre (DAM), hectometre (HOM) and kilometre (KOM) emission, the Saturn kilometric radiation (SKR), the Uranus kilometric radiation (UKR) and the Neptunian kilometric radiation (NKR) (Zarka 1998). The angular beaming of the Earth's AKR, observed with the spacecraft array Cluster (Mutel, Christopher & Pickett 2008), confirms that the Earth ECM emission pattern is strongly anisotropic. Such terrestrial coherent emission is confined within a narrow beam tangentially directed along the walls of the auroral cavity, where the amplification mechanism occurs. In the framework of the laminar source model (Louarn & Le Queau 1996a,b) such anisotropy of the ECM radiation pattern is a direct consequence of the small thickness of the cavity. In fact, the radiation path in the direction perpendicular to the cavity walls is too short to give significant amplification. The AKR will then be refracted upwards by the highest-density regions, when it leaves the cavity (Mutel et al. 2008; Menietti et al. 2011).

The auroral radio emission has also been observed in stars. In particular, such a phenomenon has been well studied in the case of CU Vir, a magnetic chemically peculiar (MCP) star. The MCPs are early type main sequence stars, characterized by strong magnetic fields with a mainly dipolar topology, whose axis is tilted with respect to the rotational axis (oblique rotator). Non-thermal incoherent radio emission from MCPs has been detected in almost 25% of cases (Drake et al. 1987; Linsky et al. 1992; Leone et al. 1994). In accordance with the oblique rotator model (ORM), the radio emission is also periodically variable as a consequence of the stellar rotation (Leone 1991; Leone & Umana 1993), suggesting that the radio emission arises from a stable rigidly co-rotating magnetosphere (RRM). This variability has been successfully reproduced by a 3D model able to compute the gyrosynchrotron emission from a RRM in the framework of the ORM (Trigilio et al. 2004; Leto et al. 2006).

The radio emission from the MCPs is ascribed to a radiatively-driven stellar wind. Far from the star, specifically on the magnetic equator at about the Alfven radius, this wind opens the magnetic field lines, forming current sheets. The reconnection of the low-strength magnetic field lines accelerates electrons up to relativistic energy. The thin transitional magnetospheric layer between the inner and dense magnetospheric regions (the region where the confined plasma accumulates) and the escaping wind is named 'middle magnetosphere'. The energetic electrons that recirculate through this layer back to the stellar surface radiate radio waves by incoherent gyrosynchrotron emission mechanism. The middle magne-

⋆ E-mail: pleto@oact.inaf.it

tosphere is also the region where the conditions for triggering the ECM mechanism could be realised. In fact, the relativistic electron population, accelerated far from the star, moves along the converging dipolar field lines toward the high-strength magnetic field regions close to the stellar surface. Moreover, due to magnetic mirroring, only energetic electrons with very low pitch-angle (electron path almost parallel to the magnetic field lines) can impact the stellar surface and will be lost. The reflected non-thermal electron population could then develop the inversion of the velocity distribution needed to trigger the ECM mechanism. Other kinds of unstable energy distribution can be developed by the precipitating non-thermal electron beams, such as the horseshoe distribution, able to efficiently produce ECM emission (Ergun et al. 2000).

In spite of the favourable physical conditions that characterize the magnetospheres of the radio MCP stars, only CU Vir and HD 133880 are so far characterized by broad-band, highly polarized and time-stable pulses (Trigilio et al. 2000, 2008, 2011; Ravi et al. 2010; Lo et al. 2012; Chandra et al. 2015), ascribed to auroral radio emission detected when the magnetic dipole axis is almost perpendicular to the line of sight. The frequency of the ECM emission observed on CU Vir ranges from about 600 MHz (Stevens & George 2010) to 5 GHz (tentative detection reported by Leto et al. 2006), whereas for HD 133880 a detection of ECM emission at 600 MHz and 1.4 GHz has been reported (Chandra et al. 2015).

CU Vir is the first star where the stellar auroral radio emission was detected (Trigilio et al. 2000). On this star, the coherent emission process was mainly observed and extensively studied at the frequencies of 1.4 and 2.5 GHz (Trigilio et al. 2000, 2008, 2011; Ravi et al. 2010; Lo et al. 2012). It shows two pulses per spin period, almost 100% right hand circularly polarized, with a phase separation of $\approx 0.4$, and characterized by a frequency drift of the pulse arrival time. Two pulses per period have been detected at 1.4 GHz in every observing epochs, unlike the auroral radio light curve at 2.5 GHz, which does not always show two pulses per period. Moreover, left-handed circularly polarized pulses were never detected from CU Vir. This lack of left-hand polarization has been explained as due to the non-perfectly dipolar topology of its magnetic field (Kochukhov et al. 2014). The existence of multipolar magnetic-field components makes the behaviour of the two opposite hemispheres asymmetric. In addition, the existence of a multipolar field topology has been indicated as the cause for the absence of auroral radio emission in $\sigma$ Ori E (Leto et al. 2012), another well-studied radio MCP star characterized by a non-simple dipole field (Oksala et al. 2012).

Similarly to the Earth AKR, the coherent pulses observed from CU Vir were explained as ECM emission originating in an auroral cavity, tangentially beamed to the walls and then upward refracted (Trigilio et al. 2011). This anisotropic beaming is able to successfully reproduce the timing and the pulse width of the auroral radio emission observed in CU Vir (Lo et al. 2012).

At the bottom of the main sequence, coherent pulses, still explained as auroral radio emission due to the ECM, were also observed in some ultra cool dwarfs (UCDs) with spectral type earlier than M7 (Berger 2002; Burgasser & Putman 2005; Antonova et al. 2008; Hallinan et al. 2008; Route & Wolszczan 2012, 2013; Williams et al. 2015), showing in some cases features similar to those observed in CU Vir. For example, the M8 dwarf DENIS-P J1048.0 – 3956 shows time-shifted pulses at 5 and 8.4 GHz, both fully right-hand circularly polarized (Burgasser & Putman 2005) and the T6.5 brown dwarf 2MASSI J1047539 + 212423 is characterized by left-hand circularly polarized periodic pulses detected at 6 GHz (Williams et al. 2015).

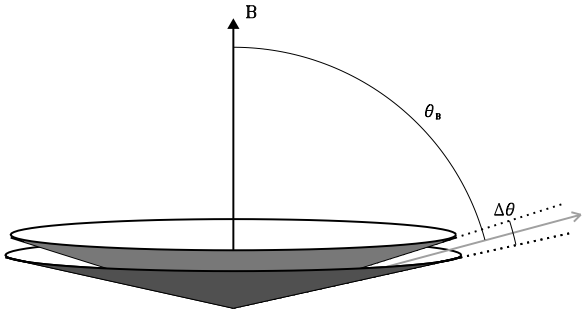


**Figure 1.** Beaming pattern of the loss-cone driven ECM elementary emission process. The amplified radiation, displayed by the light-grey vector, is emitted within an hollow-cone centered on the local magnetic field vector ($B$) of half-aperture $\theta_B$, and thickness $\Delta\theta$.

In the framework of the laminar source model, in this paper we develop a 3D-model of the auroral radio emission from stars with a dipole-like magnetic field. This model is used to study how the auroral radio-emission features depend on the stellar geometry and on the parameters that define the ECM beam pattern. This study was able to give a deeper insight about the relationship between the auroral radio emission detectability and the model parameters.

## 2 THE AURORAL RADIO EMISSION MODEL

For the ECM emission driven by the loss-cone instability, the radiation amplified by this kind of coherent emission process is beamed in a very thin hollow cone centered on the local magnetic field line (Wu & Lee 1979; Melrose & Dulk 1982). The radiation cone have half-aperture $\theta_B \approx \arccos(v/c)$, where $v$ is the speed of the unstable electrons population (Hess, Cecconi & Zarka 2008). In the case of 2 KeV energy electrons the hollow cone half-aperture is $\approx 85^\circ$. To well explain the geometry of the elementary emitting process, a thin conical sheet of thickness $\Delta\theta$ has been shown in Fig. 1. The frequency $\nu$ of the amplified radiation has to satisfy the cyclotron resonance condition for transverse emission $\nu = s\nu_B/\gamma$, where $s$ is the harmonic number of the local gyro-frequency ($\nu_B = 2.8 \times 10^{-3} B/\mathrm{G}$ GHz), for mildly relativistic electrons the Lorentz factor $\gamma \approx 1$. The fundamental harmonic ($s = 1$) has the fastest growth rate, but it is likely suppressed by the gyromagnetic absorption as it crosses the more external layer in which the second harmonic of the local gyro-frequency is equal to the amplified frequency. The layers at $s > 2$ have a lower optical depth for gyromagnetic absorption, it is thus reasonable to assume that, when detected, the ECM emission occurs at $\nu = 2\nu_B$ (Melrose & Dulk 1982).

In the case of ECM amplification occurring in thin magnetospheric cavities (laminar source model), the resulting overall radiation diagram can be strongly anisotropic (Louarn & Le Queau 1996a,b) and the axial symmetry of the single electron emission beam will be lost. In fact, the elementary ECM sources with similarly-oriented emission beam pattern and located along the line of sight contribute all together to the maser amplification. If the cavity has a laminar structure, the rays tangent to the walls maximize the path within the region where the ECM originates. Theo-

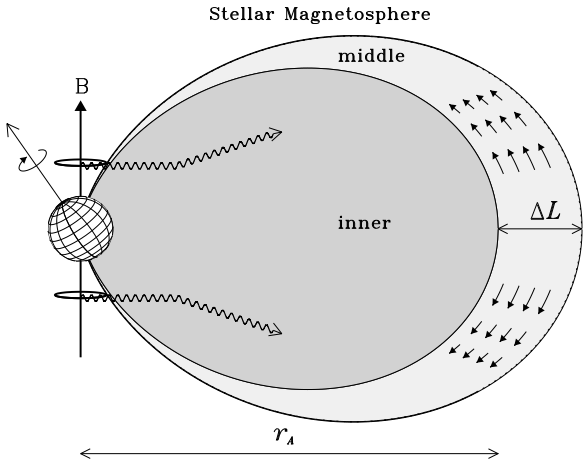


**Figure 2.** Section of a dipole-like magnetosphere, where the auroral radio emission can take place. The magnetospheric size is defined by the Alfven radius $r_A$, whereas the thickness ($\Delta L$) of the auroral cavity is defined by the lengths of the current sheet where the free electrons are accelerated up to relativistic energy. The non-thermal electrons (represented by the small solid arrows) move toward the stellar surface within a transitional layer named middle magnetosphere. Above the magnetic poles, close to the stellar surface, the two auroral rings where the ECM arises are located. The amplified radiation (the two waves displayed in the northern and southern hemispheres) is emitted tangentially to the ring and then upward refracted by the dense thermal plasma trapped inside the inner magnetosphere.

retical simulations also confirm that the auroral radio emission is mainly amplified tangentially to the cavity boundary, rather than along the perpendicular direction (Speir et al. 2014). The resulting ECM emission is beamed in a strongly directive radiation diagram and will then be detectable only when our line of sight crosses the radiation beam pattern, like the pulses of a radio light-house.

We will analyze the auroral radio emission from a dipole-like magnetospheric cavity in the framework of the laminar source model described above. The magnetosphere is assumed as a simple dipole tilted with respect to the rotation axis. Within a fixed value of the equatorial radius (Alfven radius: $r_A$), the thermal plasma accumulates (inner magnetosphere), while beyond the Alfven radius the plasma breaks the magnetic field lines giving rise to a density-depleted magnetospheric cavity (middle magnetosphere), where the non-thermal electrons can freely propagate, accelerated by magnetic reconnection (see Fig. 2). This population of non-thermal electrons can develop an unstable energy distribution, able to pump the electron cyclotron maser. The overall behavior of the ECM emission process that can take place in this kind of magnetospheric cavity (schematically pictured in Fig. 2) is described as follows: the ECM radiation arising from a generic point of the auroral ring propagates in the plane of the ring; following the laminar source model, the coherent emission is beamed along the plane parallel to the magnetic axis and tangent to the ring; then the auroral radio emission is upward refracted by the dense thermal plasma trapped within the inner magnetosphere. To study the features of the ECM pulses arising from such kind of auroral cavity, we use the same approach followed by Trigilio et al. (2004) and Leto et al. (2006). In these works, we simulated the incoherent gyrosynchrotron brightness distribution and the total flux density by sampling the space surrounding the star. Given physical parameters such us the local magnetic field strength and orientation, the thermal and non-thermal electron number density etc., we calculated at every grid point the local emission and absorption coefficients for the gyrosynchrotron mechanism, which are needed to integrate the radiative transfer equation along the line of sight. In the present work, we do not integrate the radiative transfer equation for the ECM. We only search for those spatial points that satisfy the physical conditions required for the electron cyclotron maser generation at a given frequency and that have the radiation beam pattern oriented along the line of sight. The modelling approach developed in this paper is only limited to the study of the timing and profile of the ECM pulses, which depends on those parameters that define the geometric conditions able to make such phenomenon detectable.

As a first step, we set the stellar geometry ($i$ is the inclination of the rotation axis, $\beta$ the tilt of the dipole magnetic axis, and $\Phi$ the rotation phase) and the polar field strength. The rotation axis, which is misaligned with respect to the magnetic polar axis, is displayed in Fig. 2. In the stellar reference frame, the space surrounding the star is sampled in a 3D cartesian grid and in each grid point the dipolar magnetic field vector components are calculated. The vectorial field is then rotated in the observer's reference frame (see appendix A of Trigilio et al. 2004).

As a second step, we localise the magnetospheric cavity where the unstable electron population propagates. The inner and outer boundary dipolar field lines are defined by the equation: $r = L\cos^2\lambda$, where $r$ is the distance to the centre of the star and $\lambda$ the magnetic latitude. This space region intercepts the magnetic equatorial plane at the distances $L$ and $L+\Delta L$ from the centre of the star, respectively for the inner and outer boundary. These magnetic field lines are shown in Fig. 2. Within the magnetic shell thus defined, we can find the set of grid points that have the same value of the local magnetic field strength. Given the frequency $\nu$ of the observable coherent emission we are so able to localize those grid points that have $2\nu_B = \nu$, within a fixed bandwidth $\Delta\nu$. These points are distributed in polar rings above the magnetic poles. The northern and southern auroral rings that emit the ECM at an arbitrary frequency are displayed in Fig. 2. Given the boundary magnetic field lines, the radius and height above the stellar surface of these rings follow the radial dependence of the magnetic field strength $B$, which defines the gyro-frequency.

The third step consists in the definition of the emission beam pattern of each grid point belonging to the auroral rings. For clarity, the side and top view of the ECM emission diagram arising from the northern ring are displayed in the two panels of Fig. 3. Each point of the auroral ring, which is the source of ECM emission at frequency $\nu$, has an emission diagram defined by the following angles: the deflection angle $\theta$; the opening angle $\Delta\theta$; the beaming angle $\delta$. The angle $\theta$ is defined as the angle between the ray path vector $\mathbf{k}$ and the plane containing the ring (that is perpendicular to the magnetic dipole axis). $\Delta\theta$, set equal to $5^\circ$, is the hollow-cone thickness (see Fig. 1) that in the case of the loss-cone driven instability is a function of the emitting electrons speed as $\Delta\theta \approx \nu/c$ (Melrose & Dulk 1982), and in accord with Trigilio et al. (2000) such speed has been fixed equal to $0.09c$ (electrons energy $\approx 2$ KeV), corresponding to an emitting conical sheet just $5^\circ$ thick. The angle $\delta$ accounts for the width of the radiation diagram centered on the plane tangent to the auroral circle and parallel to the magnetic axis. This angle have the aim to parameterize the number of elementary ECM sources, located in the auroral rings, with the emission beams closely aligned with the line of sight (the beam width is highlighted by the grey planes in Fig. 3). When the line of sight passing through a given grid point located on the auroral circle is tilted with respect to the local magnetic field vector of an angle

$90^\circ - \theta$ (for ECM sources in the northern magnetic hemisphere) or $90^\circ + \theta$ (for sources in the southern hemisphere) within $\Delta\theta/2$, and forms an angle lower then $|\,\delta/2\,|$ with the plane tangent to the auroral ring, the corresponding grid point will be assumed as an observable source of ECM emission.

To separate the contributions of the ECM emission arising from the two opposite magnetic hemispheres, we assign the right-hand circular polarization (RCP) to the emission from sources in the northern hemisphere and the left-hand circular polarization (LCP) to the emission from the southern ones. If we repeat the operations explained above as a function of the stellar rotation phase and store the number of grid points that are ECM sources, along with their corresponding polarization sense, then we are able to simulate the features of the ECM light curves for the I and V Stokes parameters (respectively defined as RCP + LCP and RCP − LCP).

As a further output, once we set the stellar parameters that describe the geometry and strength of the dipolar field, the 3D-model provides us with the effective magnetic field curve. In fact, the simulations of the ECM emission require the calculation of the vectorial field generated by the magnetic dipole. For a given rotational phase, we are able to calculate the longitudinal component of each magnetic field vector located on the stellar surface. The sum of such longitudinal components, weighted by the limb darkening law, gives us the theoretical effective magnetic field strength ($B_\mathrm{e}$) as a function of the stellar rotation. In detail, such calculation has been performed as follow:

$$B_\mathrm{e} = \frac{\sum_x \sum_y \sum_z B_\mathrm{x}(x,y,z) I(x,y,z)}{\sum_x \sum_y \sum_z I(x,y,z)}$$

where $B_\mathrm{x}$ is the longitudinal component of the magnetic field vector located at the coordinate $(x,y,z)$ in the side of the stellar surface facing to the observer, and $I$ is the corresponding limb darkening parameter. The observing reference frame ($Oxyz$) is centered on the stellar center, the $x$-axis is aligned with the line of sight and oriented toward the observer, the $y$ and $z$-axes individuate the plane of the sky. Each point of the grid is associated to the vector $\vec{r} \equiv (r_\mathrm{x}, r_\mathrm{y}, r_\mathrm{z})$, and the points located on the stellar surface are those that verify, within the sampling step, the condition $r_\mathrm{x}^2 + r_\mathrm{y}^2 + r_\mathrm{z}^2 = 1$ (assuming a unitary stellar radius). For the calculation has been adopted the simple linear limb darkening law:

$$I(x,y,z) = 1 - k + k r_\mathrm{x}(x,y,z) \qquad (0 \leqslant r_\mathrm{x} \leqslant 1)$$

with $k = 0.45$ (Stift 1973). Therefore, with the capability to simultaneously simulate the ECM light curve and the magnetic curve, we can correlate the ECM occurrence with the $B_\mathrm{e}$ curve.

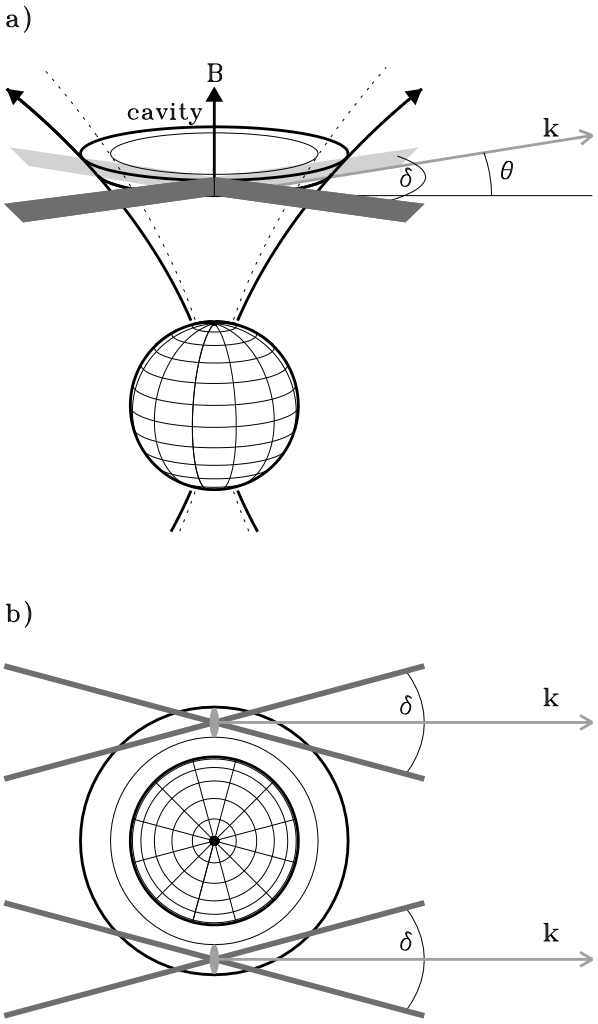


**Figure 3.** Schematic view of the model of the auroral radio emission developed in the framework of the laminar source model. Panel a) side view; panel b) top view. The density-depleted magnetic cavity and the boundary field lines are shown. A representative auroral ring is also displayed above the north pole, where the ECM emission process originates. The grey planes passing trough the boundary of the cavity describe the ECM beam pattern, whose size is given by the angle $\delta$. The ECM ray vector ($k$) is misaligned of an angle $\theta$ with respect to the direction perpendicular to the local magnetic field vector ($B$).

## 3 MODEL PREDICTIONS

### 3.1 Dependence on the auroral ring geometry

First of all we analyze if the spatial location and the size of the auroral regions that are sources to the ECM emission affect the simulated light curves. To do this, we set the magnetic field and vary the frequency; this is equivalent to simulate ECM emission from auroral rings of different sizes and locations above the stellar surface.

We simulated a set of frequencies ranging from 600 MHz to 5 GHz. For this specific analysis the stellar geometry and the ECM radiation diagram are fixed. We assumed a dipole with a polar field strength of 3000 gauss, misaligned with respect to the rotation axis of an angle $\beta = 74^\circ$, the rotation axis inclination ($i$) has been fixed to $43^\circ$. The parameters above are equal to the stellar parameters adopted for CU Vir (the prototype of the stars showing auroral radio emission) by Trigilio et al. (2000). The thickness of the magnetic shell that delimits the auroral cavity has been defined setting the $L$-shell parameter of the two boundary dipolar magnetic field lines, respectively equal to 15 and 18 $\mathrm{R}_*$ ($\Delta L = 20\% L$), in accordance with the size of the magnetospheric region, where the incoherent radio emission of CU Vir originates (Leto et al. 2006). The two boundary magnetic field lines have the maximum separation at the magnetic equator, whereas at the stellar surface these two field lines are very close. For the ECM emission beam pattern, we assume the simple condition of amplified radiation propagating perpendicularly to the local magnetic field vector (no refraction, $\theta = 0^\circ$) with a narrow radiation diagram (opening angle fixed to $\delta = 10^\circ$).

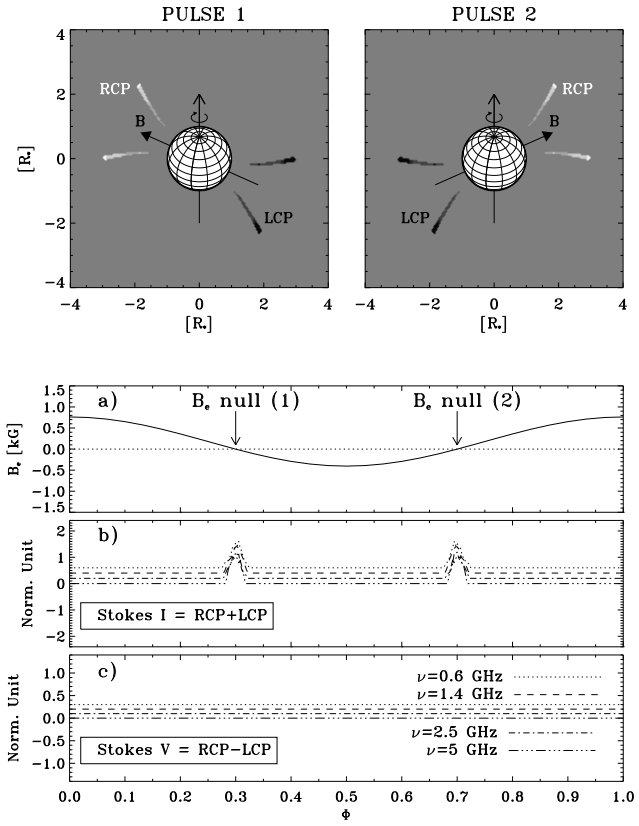


**Figure 4.** Top panels: wide band synthetic brightness spatial distribution of the ECM emission arising from the two opposite hemispheres of a dipole-like oblique rotator. The maps have been created for the two stellar orientations where the longitudinal magnetic field is null. The simulated frequencies range between 5 GHz, close stellar regions, and 600 MHz, farther regions. The emission that originates from the northern hemisphere is shown by the white area, while the dark area is associated to the ECM emission from the southern hemisphere. Bottom panel a): simulated magnetic curve. Bottom panel b) and c): ECM light curves simulated at $\nu = 0.6$, 1.4, 2.5 and 5 GHz, respectively for Stokes I and V. An arbitrary offset has been added to each individual light curve to distinguish them.

The spatial distribution of the ECM emission, calculated when the magnetic dipole axis lies exactly in the sky plane (null value of the effective magnetic field), has been displayed in the top panels of Fig. 4. The simulated maps were obtained by collecting the ECM contributions from all grid points (simulation step equal to 0.05 $R_*$) that have the second harmonic of the local gyrofrequency in the range from 600 MHz to 5 GHz.

In accordance with the radial dependence of the magnetic field strength, decreasing outward as $r^{-3}$ for a dipole, the highest frequencies originate in small auroral rings located near the star, the low frequencies are instead generated in large auroral rings at high distance above the stellar surface. The simulated frequencies originate from auroral rings located between $\approx 0.5$ and 2 $R_*$ from the stellar surface. The ECM emission at 5 GHz is generated within the thin auroral cavity located close to the star, unlike the ECM radiation at 600 MHz, which arises from the auroral regions far from the star, and is consequently generated within a larger and thicker auroral cavity.

The model predicts similar ECM light curves at different simulated frequencies (small differences are due to the sampling effect) characterized by two peaks per stellar rotation, visible when $B_e = 0$. The theoretical magnetic curve and the corresponding ECM light curves for the Stokes I and V are displayed in the three bottom panels of Fig. 4, simulated setting $\nu = 0.6$, 1.4, 2.5 and 5 GHz. As a consequence of the chosen stellar geometry (assumed equal to the prototype CU Vir), the minimum phase difference between the two simulated ECM peaks is about 0.4, that is in accordance with the phase difference between the two coherent events observed on CU Vir.

By inspecting the simulated light curves for the two Stokes parameters, we can notice that there is not any Stokes V (RCP $-$ LCP) contribution, whereas the Stokes I (RCP $+$ LCP) is well observable. This is because the ECM contributions from the two opposite magnetic hemispheres are exactly the same, as it is evident by the perfect symmetry of the ECM brightness spatial distribution (top panel of Fig. 4). Since the ECM radiation arising from the two hemispheres has opposite polarization senses in the north and in the south, the Stokes V parameter will be consequently null.

### 3.2 Dependence on the beam pattern

To assess the effect of the free parameters that control the beam pattern of the ECM radiation on the auroral radio emission features, we simulated the light curves varying the opening angle $\delta$, and the upward deflection angle $\theta$, keeping the stellar geometry previously adopted. In this case, we performed simulations of the ECM emission at 2.5 and 1.4 GHz. To mitigates the possible bandwidth effect that could affect the comparison between the simulations and most of the available observations, these simulations have been performed within a narrow frequency range, 100 MHz wide, which is close to the old VLA and ATCA bandwidth set-up. For the assumed polar field strength ($B_e = 3000$ Gauss), the two auroral rings are located respectively at $\approx 0.9$ and 1.3 $R_*$ above the magnetic poles. The results of the simulations for the Stokes parameter I and V are displayed in Fig. 5, where the right circularly polarized emission (positive Stokes V) is displayed in white and the left circularly polarization (negative Stokes V) in black. In each panel of Fig. 5, for a given angle $\delta$, the dynamical simulated light curves are displayed as a function of the angle $\theta$, shown on the $y$-axis.

First of all, we notice that the light-curve features of the auroral radio emission at the two simulated radio frequencies - 1.4 and 2.5 GHz - have a closely similar dependence on the two parameters $\delta$ and $\theta$. This is equivalent to say that the spatial location and the size of the auroral rings have little or no effect on the main features of the auroral radio emission, once the auroral cavity is defined. The timing and the pulse profile are instead significantly affected by the choice of $\delta$ and $\theta$. In particular, the dynamic light curves of the Stokes I parameter show that the pulse width is directly related to the angle $\delta$, with the narrow peaks associated to the smaller $\delta$ values. We also note that the pulses disappear above a deflection angle limit. This trend is observable for each value of the parameter $\delta$, with the limit value of the angle $\theta$ growing as $\delta$ increases. It is also evident that, before disappearing, each pulse splits in two, with phase separation growing with $\theta$. By analyzing the Stokes V, it is clear that each component of the double peak pulses has opposite polarization sense. In general, Stokes V has a hybrid polarization, as a consequence of the different contributions to the ECM emission of the two stellar hemispheres with opposite magnetic polarity. As a consequence of the physical processes that are responsible of the generation and propagation of the ECM emission, the deflection angle $\theta$ could be a function of the frequency. In fact,

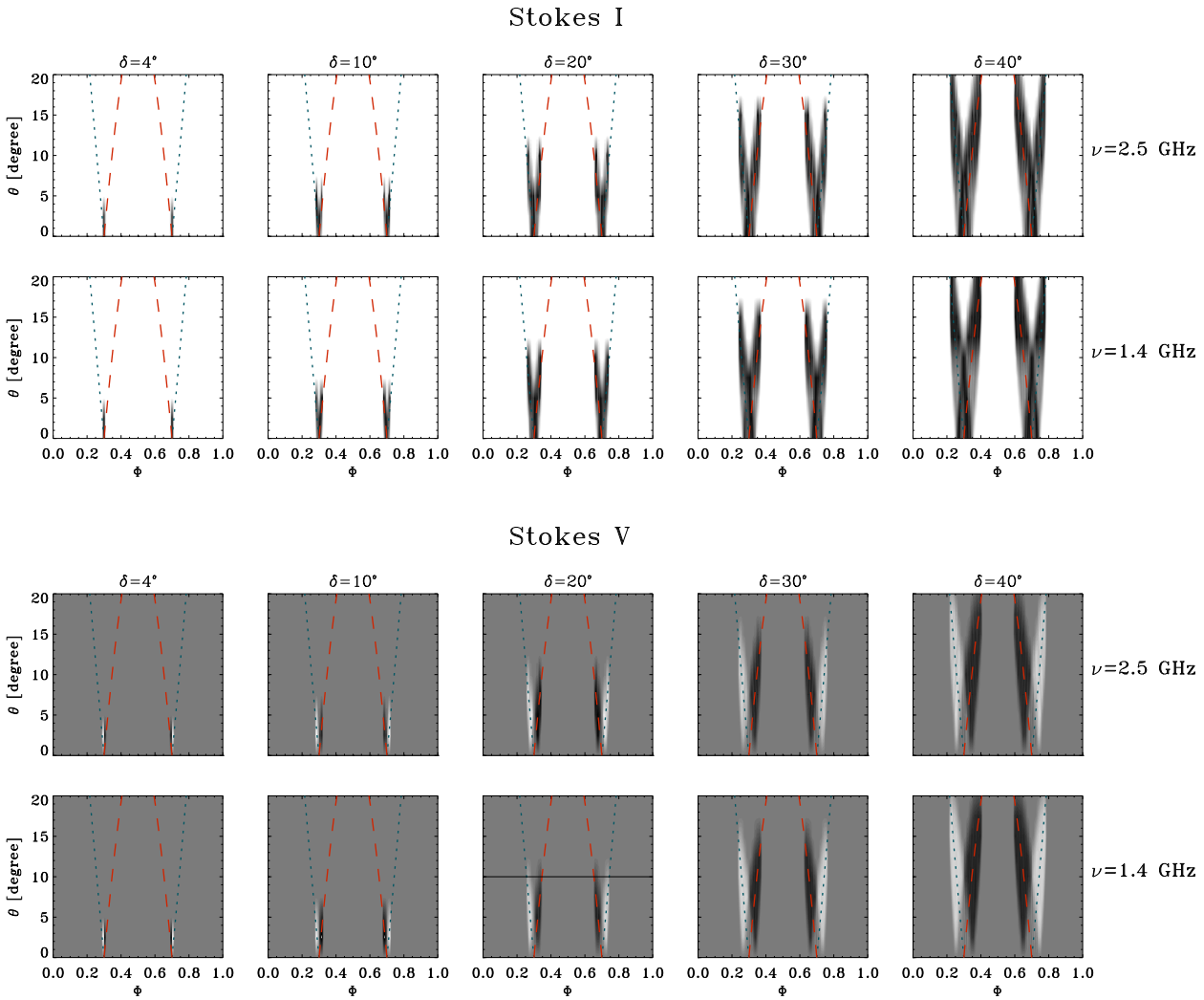


**Figure 5.** Dynamic ECM light curves results of the 3D model simulations obtained varying the parameters that control the radiation beam pattern. The simulated frequencies are: 1.4 and 2.5 GHz. The model simulations have been performed as a function of the ray path deflection $\theta$, y-axis of each panel. The simulations have been performed for 5 values of the opening angle $\delta$. The top panels display the Stokes I parameter, while the bottom panels display Stokes V; black corresponds to the left handed circularly polarized component, white indicates right hand polarized. The pulse phase location predicted by the ORM have also been shown; the blue dotted line is related to the ECM pulses arising from the northern hemisphere, the red dashed line is referred to the southern. The black continuous line in the panel with the simulations performed at $\nu = 1.4$ GHz and $\delta = 20^\circ$ is a representative light curve obtained assuming $\theta = 10^\circ$.

the basic processes that drive the ECM, like the loss-cone instability, originate amplified radiation propagating in direction which is frequency-dependent, or/and the refraction effects, that can be suffered by the amplified radiation traveling through the cold thermal plasma layers that are located in the stellar magnetosphere, which are also function of the frequency. Comparing multi frequency observations and simulations we will be able to measure the deflection angle of each individual amplified frequency, and thus we can try to disentangle among the possible frequency-dependent mechanism that can affect the propagation direction of this kind of amplified emission.

The pulse timing is the result of the oblique rotator model assumption. In fact, the upward deflection angle $\theta$ is related to the angle formed by the line of sight with the magnetic dipole axis ($\theta_{\rm M}$) as follows:

$$\theta_{\rm M} = \begin{cases} \pi/2 - \theta & \text{Northern Hemisphere} \\ \pi/2 + \theta & \text{Southern Hemisphere} \end{cases}$$

Once the ORM geometry ($i$ and $\beta$) is defined, the phase location of the ECM pulse is expressed by the following equation (Trigilio et al. 2000):

$$\Phi_{\rm ECM} = \arccos\left(\frac{\cos\theta_{\rm M} - \cos\beta\cos i}{\sin\beta\sin i}\right)/2\pi \qquad (1)$$

The tracks of the ECM pulses calculated by the use of Eq. 1 have been put on top of the simulated light curves in Fig. 5. The comparison between the model simulation and the ORM prediction indicates that the phase location of each ECM peak can be predicted by Eq. 1, whereas the ECM pulse profile is the result of a complicated combination of the angles that control the beam of the auroral radio emission.

To better clarify the above model prediction, the 1.4 GHz

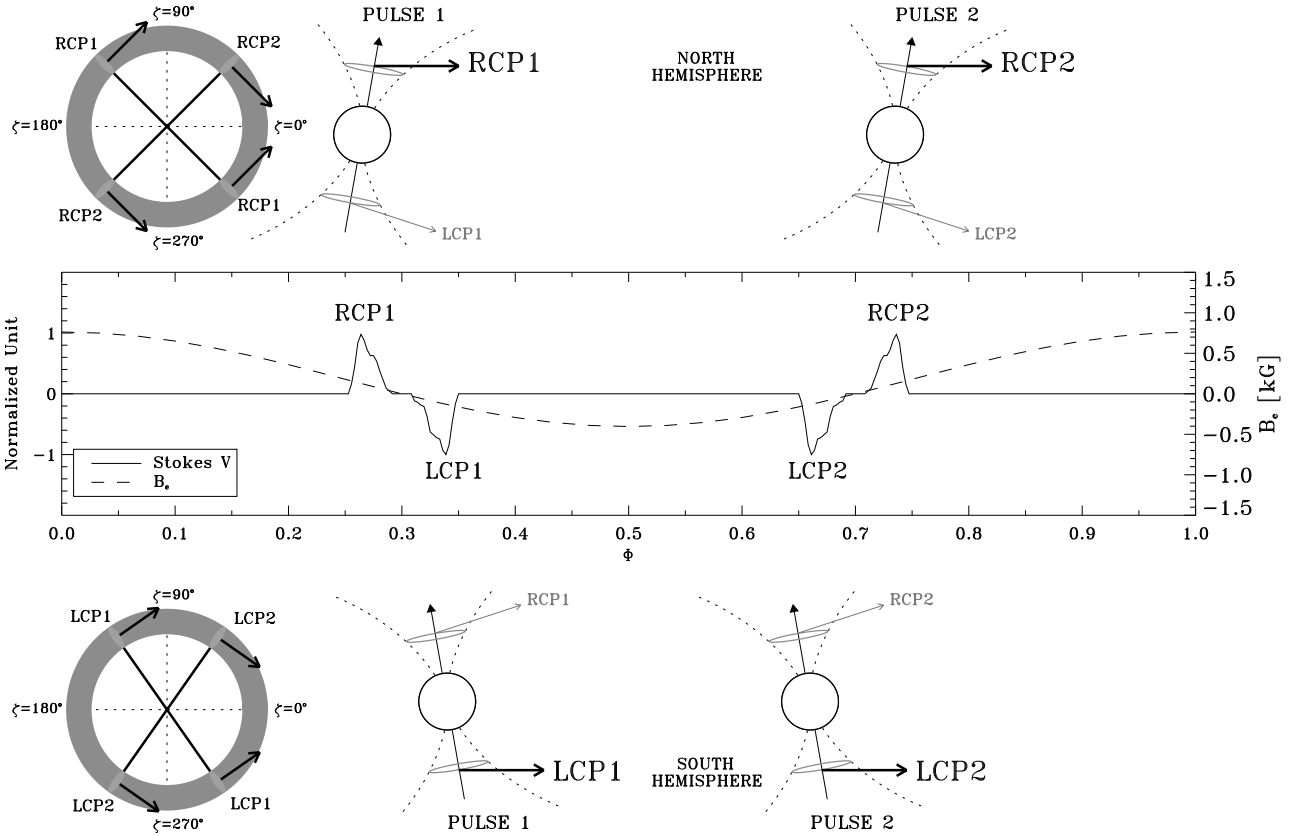


**Figure 6.** Synthetic auroral radio light curve (obtained assuming: $\nu = 1.4$ GHz, $\delta = 20^\circ$ and $\theta = 10^\circ$), solid line, with superimposed the simulated effective magnetic field curve ($B_p = 3000$ Gauss, $i = 47^\circ$, $\beta = 74^\circ$), dashed line. The pulses have been labelled as in Fig. 4 according to the arrival order and the circular polarization signs. The cartoons show the magnetosphere orientations corresponding to the beam of the auroral radio emission aligned with the line of sight. The two unit circles indicate the magnetic longitudes ($\zeta$) of the magnetic field lines responsible of the auroral radio emission observable from Earth.

stokes V synthetic light curve obtained with $\delta = 20^\circ$ and $\theta = 10^\circ$ has been analysed (it is identified in Fig. 5 by the black line). This selected light curve is shown in Fig. 6 along with the stellar magnetic curve. The stellar orientations associated with the various pulse components and identified on this simulated light curve have also been displayed. For clarity, each pulse component has been assigned a label related to the order of appearance and to the polarization sense. The ECM ray vectors have been tagged according to the labels of the corresponding simulated coherent pulse components.

The ECM emission beam pattern responsible for the first right-hand circularly polarized peak (RCP1) arising from the northern auroral ring is aligned with the line of sight at phases slightly preceding the first null of the magnetic curve, depending on $\theta$ (Fig. 6). As the star rotates, the northern pole will be seen moving away from the observer and, after the magnetic curve passes the first null, the ECM emission arising from the southern auroral ring will be visible (first left-hand circularly polarized pulse: LCP1). As the star rotates, after that the magnetic curve has reached its negative magnetic outermost point, the magnetic north pole will be seen approaching the observer and a second ECM beam generated from the southern auroral ring will be aligned with the line of sight. Consequently, the second LCP pulse will be detectable (LCP2). Likewise, the second RCP pulse will be associated to a second ECM beam arising from the northern auroral ring (RCP2).

The two ECM beams are not arising from the same points of the auroral circle. For clarity, in Fig. 6 we also included the auroral circles showing the magnetic longitudes $\zeta$ ($\zeta = 0^\circ$ on the the plane identified by the magnetic and rotation axis) of the magnetic field lines responsible for the detectable auroral radio emission. Such magnetic field lines intercept the northern and the southern auroral rings in the two sectors characterized by ECM beam pattern crossing the observer's line of sight. In particular, for the specific case analysed here, the magnetic longitudes of the field lines that have the most favourable orientation for the auroral radio emission to be detected are respectively: $\zeta \approx 135^\circ$ and $\zeta \approx 315^\circ$ (peak RCP1); $\zeta \approx 45^\circ$ and $\zeta \approx 225^\circ$ (peak RCP2); $\zeta \approx 125^\circ$ and $\zeta \approx 305^\circ$ (peak LCP1); $\zeta \approx 55^\circ$ and $\zeta \approx 235^\circ$ (peak LCP2).

### 3.3 Dependence on the magnetic shell size

We performed model simulations of the auroral radio emission arising from magnetic shells with sizes different from the one previously analysed. The simulated ECM frequency and the radiation beam pattern were left unchanged ($\nu = 1.4$ GHz, $\delta = 20^\circ$ and $\theta = 10^\circ$). We analyse the cases of auroral cavities delimited by the inner boundary magnetic field lines with the $L$-shell parameter ranging from 5 to 100 $R_*$. In addition, the magnetic shell thickness at the equatorial plane has been varied in the range from 10% to 50% of the $L$ parameter of the inner boundary magnetic field line.

The simulated dynamic ECM light curves (Stokes I and V) as a function of the auroral cavity size have been displayed in Fig. 7. Each column panels of Fig. 7 show the simulations performed assuming different thickness of the magnetic cavity. Similarly to the

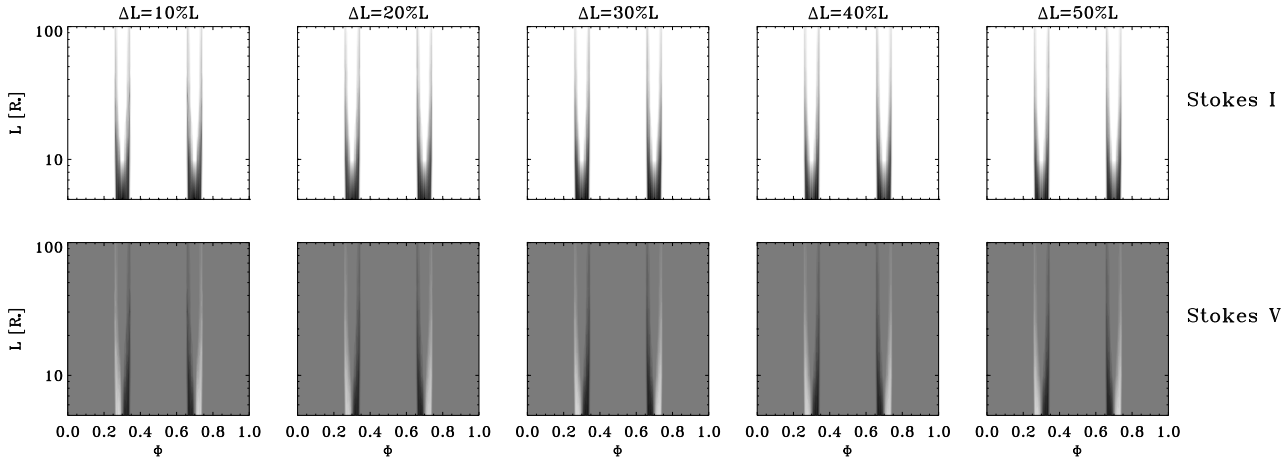


**Figure 7.** Dynamic auroral light curves as a function of the magnetic shell size. Top panels: Stokes I; middle panel: Stokes V. The simulations have been performed varying the equatorial extension of the magnetospheric cavity where the auroral radio emission takes place (defined by the *L*-shell parameter), and the corresponding shell thickness.

previously adopted grey scale for the Stokes V simulations, the white regions indicate the ECM emission that have a right hand circular polarization sense, whereas the black areas refer to radiation with left-hand circular polarization.

The result of these simulations highlights that the size of the auroral cavity significantly affects the pulse profile. The simulations of the auroral radio emission for the Stokes I arising from small magnetic shells are characterized by two large pulses per stellar rotation, see top panels of Fig. 7. As the size of the magnetic shell increases, the two simulated pulses become clearly doubly peaked, each single peak becoming progressively thinner. Each component is clearly related to a specific stellar hemisphere, as recognizable from the sign of the simulated light curves for the Stokes V in the middle panels of Fig. 7. The thinning of the pulse with the increasing magnetic shell size is the consequence of the progressive decrease of the auroral ring radius associated to a specific radio frequency (as extreme case, for a magnetic shell with infinite *L*-shell parameter the auroral region degenerates to a point located on the magnetic axis), and consequently the number of grid points that are sources of detectable ECM emission progressively decreases. This set of simulations highlights that the ECM features do not depend on the ratio $\Delta L/L$.

### 3.4 Dependence on the stellar geometry

To highlight the role of the stellar geometry on the auroral radio emission detectability, a set of model simulations have been performed by varying the angle $\beta$. After setting the auroral shell size ($L = 15$ R$_*$ and $\Delta L = 20\% L$), we performed simulations at $\nu = 1.4$ GHz (beam pattern defined by $\delta = 20^\circ$ and $\theta = 10^\circ$), varying the magnetic axis obliquity ($\beta$) from 0° to 360° (with a simulation step of 1°). The magnetic polar strength and the rotation axis inclination were left unchanged ($B_\mathrm{p} = 3000$ Gauss, $i = 43^\circ$).

The variation of the $\beta$ parameter significantly affects the features of the ECM light curves and the stellar magnetic field curve. We then compared the simulated ECM light curves with the corresponding effective magnetic field curve. The dynamic light curves and the magnetic curves are displayed in Fig. 8 as a function of $\beta$. The effective magnetic field is displayed in the top panel of the figure and the other two panels show the Stokes I and V auroral radio emission (respectively, bottom and middle panels of Fig. 8).

By looking at Fig. 8, it is evident that the ECM light curve features depend on the adopted stellar geometry. In particular, the detectability of the auroral radio emission and the phase separation between the two simulated pulses is a function of $\beta$. When the magnetic axis is aligned with the rotation axis ($\beta = 0^\circ$ or $\beta = 180^\circ$) the effective magnetic field does not vary. The effective magnetic field strength has a positive constant value for $\beta = 0^\circ$ (northern hemisphere prevailing), negative value for $\beta = 180^\circ$ (southern hemisphere prevailing). When the magnetic obliquity increases, the effective magnetic field changes as the star rotates. For $\beta = 90^\circ - i = 47^\circ$, the magnetic field curve is characterized by one null at $\Phi = 0.5$. When $\beta$ is close to this value, the light curve of the auroral radio emission is characterized by only one pulse per stellar rotation, right-hand circularly polarized, centred at $\Phi = 0.5$. As the magnetic obliquity increases, the effective magnetic field inverts its sign twice at every stellar rotation. Therefore, we simulated two doubly peaked ECM pulses.

At $\beta = 90^\circ$, the pulse separation increases up to $\Delta\Phi = 0.5$, where it starts to decrease. For $\beta = 180^\circ - i = 133^\circ$, the magnetic field curve has again a single null, but at $\Phi = 0$. When the misalignment between magnetic and rotation axis is close to this value, the light curve of the auroral radio emission shows a single large pulse, left-hand circularly polarized and centred at $\Phi = 0$. Beyond this limit of $\beta$, the auroral radio emission vanishes. The exact limits of the range of $\beta$ able to give detectable auroral radio emission also depend on the ray path deflection $\theta$. The simulations performed when $\beta$ lies in the range 180°–360° closely resemble the behaviour simulated in the range 0°–180°, but with the opposite sign of $B_\mathrm{e}$. Consequently, a swap of circular polarization occurs (middle and top panel of Fig. 8). As a result of the present analysis, it can be noticed that the capability to detect the ECM radiation is marginal for those stars that do not change their net polarity of the effective magnetic field on the observer's line of sight.

The beam pattern chosen to perform the present analysis is up-ward deflected. The simulated ECM radio light curves are then characterized by contributions from the two opposite hemispheres that are clearly distinguishable by the sign of the simulated Stokes V parameter. If the ray path is not deflected ($\theta = 0$), the simulated

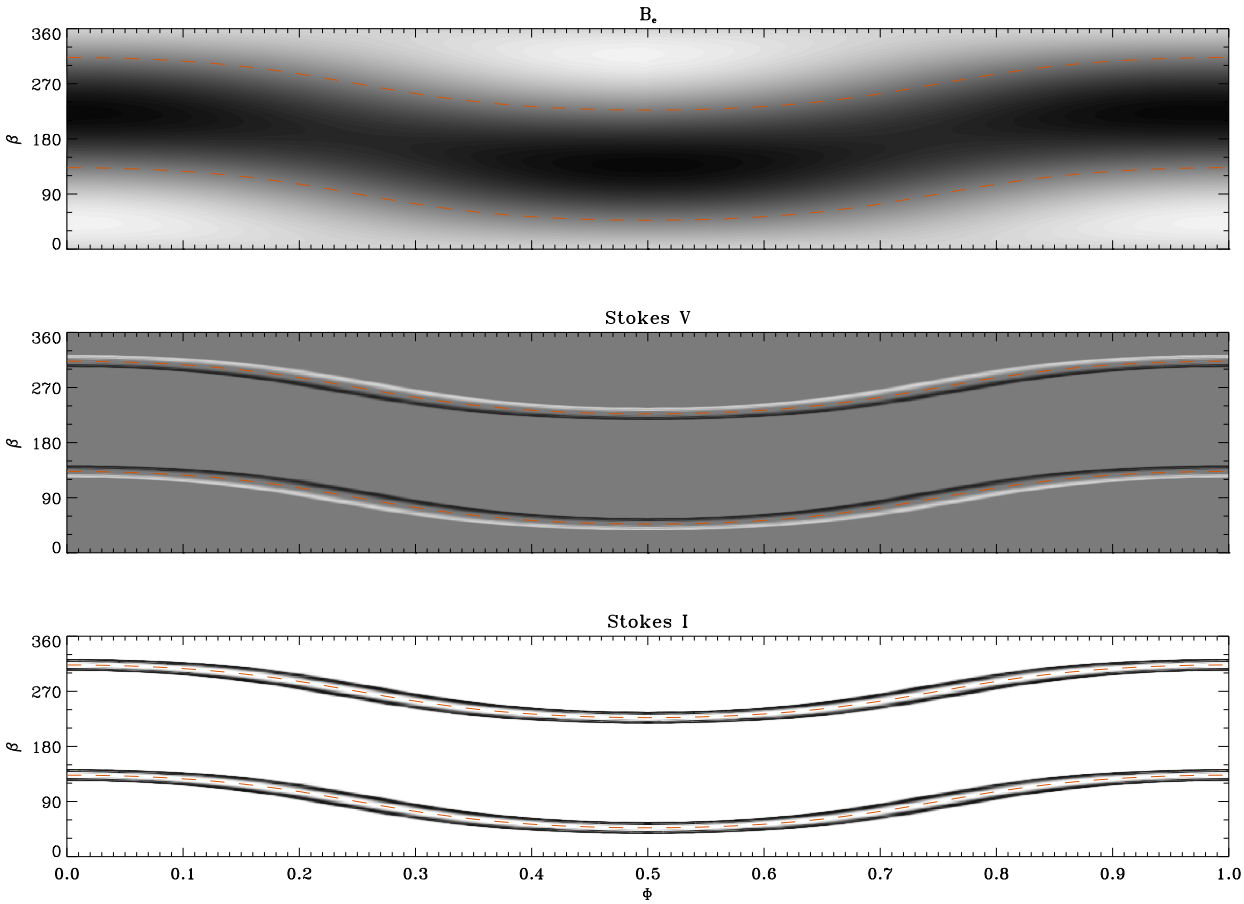


**Figure 8.** Variations of the effective magnetic field curve and of the auroral light curve as a function of the misalignment between the magnetic and the rotation axis orientations (angle $\beta$). Top panel: dynamic effective magnetic field curves. Middle panel: dynamic auroral light curves for the Stokes V. Bottom panel: dynamic auroral light curves for the Stokes I. The orange dashed lines indicate the values of $\beta$ that locate the nulls of the magnetic effective curve at fixed values of the stellar rotational phase, obtained using the Eq. 2.

auroral radio emission is unpolarized (Stokes V$=0$). The Stokes I light curve is instead characterized by two single peaks occurring at phases ($\Phi_0$ and $1-\Phi_0$), which represent the stellar orientations characterized by the magnetic axis being perpendicular to the line of sight ($B_e = 0$), according to the analysis performed in Sec. 3.1. In this case, the detection of the auroral radio emission from a star can be used to fix the oblique rotator geometry ($\beta$), the rotation axis inclination $i$ being known. In fact, on the basis of the simple dipolar geometry, from the Eq. 1 the following relation can be derived:

$$\beta = \arctan\left(-\frac{1}{\tan i \cos\Phi_0}\right) \quad (2)$$

Given the rotation axis inclination, the equation above returns those value of $\beta$ for which the effective magnetic field curve is zero at $\Phi_0$. The results of the Eq. 2, obtained assuming $i = 43^\circ$, have been superimposed on the model simulation in Fig. 8. It can be noticed that the curves $\beta$ versus $\Phi_0$ are intermediate between the tracks left by the characteristic double peaks of opposite polarity, which are a signature of deflected ECM emission (middle and bottom panels of Fig. 8). Therefore, in the case of auroral radio emission characterized by ray path deflection ($\theta > 0$), it is also possible to obtain the ORM geometry. This is because if the ECM contributions arising from the two opposite stellar hemispheres are clearly detected, then the stellar rotational phase related to a null of the effective magnetic field can be located in the middle between the phases of occurrence of the coherent peaks with opposite Stokes V sign.

## 4 DISCUSSION AND CONCLUSIONS

The purpose of the model described in this paper is the simulation of the auroral radio emission from stars characterized by a dipole-like magnetic field. The auroral radio emission is a well-known phenomenon common to the magnetized planets of the solar system (Zarka 1998), and also present in some kinds of magnetic stars (Trigilio et al. 2011; Nichols et al. 2012). The mechanism responsible for this kind of radio emission is the coherent amplification mechanism known as ECM. The modelling of the ECM emission has been developed in accordance with the laminar source model (Louarn & Le Queau 1996a,b). In this case, the auroral radio emission is constrained within a narrow beam tangentially directed along the cavity boundary. This kind of anisotropic beaming is able to successfully reproduce the timing and the pulse width of the auroral radio emission observed from the early type star CU Vir (SP A0V) (Trigilio et al. 2011; Lo et al. 2012). Moreover, at the bottom of the main sequence, the presence of ECM emission characterized by strongly anisotropic beaming has been confirmed in the case of the ultra cool dwarfs (SP $>$ M7) (Lynch, Mutel & Güdel 2015).

The dependence of the auroral radio emission features on the model parameters has been extensively analysed. Despite the simplified assumption of a pure dipole characterizing the stellar magnetic field, this model is a powerful tool to study how the timing and the pulse profile depend on the parameters that define the source geometry and on the parameters that control the beam pattern. The analysis in this paper allows us to draw some general conclusions that help us to interpret the features observed in the auroral radio emission from individual stars.

First of all, we point out how the recurrence phases of the ECM pulses are related to the features of the magnetic curve. In the cases of the auroral radio emission propagating perpendicularly to the magnetic field vector, we obtain unpolarized coherent pulses coinciding exactly with the nulls of the effective magnetic field curve, since RCP and LCP rays have the same direction. This coincidence ceases as the ECM beam pattern deflects. In this case, each single auroral radio pulse becomes doubly peaked, because the two polarizations are deflected differently. As a consequence of the magnetic polarity of the stellar hemisphere where the ECM emission arises, the peak components are circularly polarized with opposite polarization senses.

In particular, the two components of opposite polarization sense occur at phases slightly preceding or following the effective magnetic field null. The phase separation between the two polarized components can be a function of such model parameters as the ray path deflection, the beam opening angle, or the magnetic shell size. In all cases, the two components are symmetric with respect to the magnetic field null phase.

As a further result of our simulation, we found that once we set the size of the magnetic shell where the auroral radio emission takes place, the distance from the surface, hence the size of the auroral ring, does not affect the simulated pulse profile and their localization in phase. It has also been established that the magnetic shell thickness has negligible effects on the light-curve features. Moreover, the size of the magnetic shell does not affect the timing of the auroral pulses, while it does have an influence on the pulse profile. In particular, if the auroral radio emission is generated very close to the magnetic dipole axis, as in the case of the very small auroral rings related to large magnetospheric shells, the ECM arising from each stellar hemisphere has a very narrow pulse width. We can conclude that, once defined the magnetic shell and fixed the beaming of the ECM emission, all the auroral radio frequencies that originate from regions located at different heights above the stellar surface are characterized by similar light curves. About the model parameters analyzed above, we can conclude that the auroral radio emission features are frequency independent. In the sense that, once fixed the parameters that control the beam pattern, the location above the poles of the auroral rings, that are frequency dependent, have no effect on the modeled auroral radio emission. However, as discussed below, other frequency dependent effects can take place on the ECM stellar radio emission. Moreover, the ECM beam pattern is reasonably related to the auroral ring geometry, roughly speaking auroral radio emission detectable in direction strongly misaligned from the plane tangent to the cavity wall should be generated in large thickness auroral ring, conversely strongly beamed ECM emission is related to very thin auroral cavity.

The discovery that the light curve of the auroral radio emission does not depend on the height above the surface of the auroral ring where it originates has a direct implication on the parameters that are able to locate it. These parameters are the polar magnetic field strength and the harmonic of the gyrofrequency amplified by the ECM process. From the analysis performed in this paper, it follows that the above parameters cannot be directly deduced only from the detection of the auroral radio emission from a given star.

The measurement of possible frequency-dependent effects of the pulsed auroral radio emission, such as the frequency drift of the pulses' arrival time, has to be related to a possible propagation effect suffered by the auroral radio emission generated at different frequencies (for example, the ambient thermal medium refracts differently the ECM radiation of different frequencies, as proposed by Trigilio et al. 2011), or to the intrinsic nature of the basic process that generates the ECM amplified radiation (for example, in case of the loss-cone driven ECM emission the hollow cone opening angle is a function of the frequency). In detail, the half-aperture of the hollow cone is defined as follow: $\cos\theta_{\rm B} = \nu/c\sqrt{1-\nu_{\rm B}/\nu_{\rm B_{max}}}$ (Hess et al. 2008), where, following the resonance condition for the gyromagnetic emission at the $s$-th harmonic, $\nu_{\rm B} = \nu/s$ (Melrose & Dulk 1982), with $\nu_{\rm B_{max}}$ the gyrofrequency at the stellar surface. We note how the elementary process which gives rise to the amplified radiation could affect the propagation direction of the resulting auroral radio emission detected at different frequencies. On the other hand, the ECM radiation, originated in a density depleted region close to the stellar surface, along its path passes through refracting cold thermal regions that deflect the propagation direction. The ray path refraction is described by the law of Snell: $\sin\alpha_{\rm r} = \sin\alpha_{\rm i}/n_{\rm refr}$, where $n_{\rm refr} = \sqrt{1-\nu_{\rm p}^2/(\nu(\nu-\nu_{\rm B}))}$ is the refraction index of the cold thermal medium traveled by the amplified rays, and $\alpha_{\rm i}$ and $\alpha_{\rm r}$ are the angles that the incident and the refracted rays form with the line perpendicular to the refractive layer. The refraction plane orientation depends on the shape of such refractive layers, this can introduce a possible further longitudinal deflection to the ray path giving rise to a possible phase shift of the coherent pulses. Moreover, the plasma frequency depends from the density of the thermal plasma ($N_{\rm e}$) as follow: $\nu_{\rm p} = 9\times10^{-6}\sqrt{N_{\rm e}}$ GHz, a possible longitudinal anisotropy of the ambient thermal medium, trapped within the stellar magnetosphere, could affect the propagation of the two ECM pulses differently. We highlight that the comparison among the magnetic curve and the Stokes I and V light curves of the auroral radio emission can be used as a diagnostic tool of the environment where the ECM is pumped.

Finally, the simulations performed here allow us to highlight that the main parameter that localizes the auroral radio pulses in the phase-folded light curve is the obliquity of the stellar magnetosphere with respect to the rotation axis. As expected, the timing of the auroral radio pulses is strictly related to the geometry of the star. Moreover, the magnetic axis orientation is strictly related to the possibility to detect such a phenomenon. We can conclude that the study of the timing of the ECM pulses from stars that show such an elusive phenomenon could be a very useful tool to obtain hints about the geometry of the magnetosphere where it takes place, besides its extraordinary importance in the study of the physical conditions able to generate the ECM radiation itself.

**ACKNOWLEDGMENTS**

We thank the referee for his/her constructive criticism which enabled us to improve this paper.

**REFERENCES**


Antonova A., Doyle J.G., Hallinan G., Bourke S., Golden A., 2008, A&A, 487, 317

Berger E., 2002, ApJ, 572, 503

Burgasser A.J., Putman M.E., 2005, ApJ, 626, 486

Chandra P., Wade G.A., Sundqvist J.O., et al., 2015, MNRAS, 452, 1245

Ergun R.E., Carlson C.W., McFadden J.P., Bieging J.H., Delroy G.T., 2000, ApJ, 538, 456

Drake S.A., Abbot D.C., Bastian T.S., Bieging J.H., Churchwell E., Dulk G., Linsky J.L., 1987, ApJ, 322, 902

Hallinan G., Antonova A., Doyle J.G., Bourke S., Lane C., Golden A., 2008, ApJ, 684, 644

Hess S., Cecconi B., Zarka P., 2008, GeoRL, 35, 3107

Kochukhov O., Lftinge T., Neiner C., Alecian E., and the MiMeS collaboration, 2014, A&A, 565, 83

Leone F., 1991, A&A, 252, 198

Leone F., Umana G., 1993, A&A, 268, 667

Leone F., Trigilio C., Umana G., 1994, A&A, 283, 908

Leto P., Trigilio C., Buemi C.S., Umana G., Leone F., 2006, A&A, 458, 831

Leto P., Trigilio C., Buemi C.S., Leone F., Umana G., 2012, MNRAS, 423, 1766

Lynch C., Mutel R.L., Güdel M., 2015, ApJ, 802, 106

Linsky J.L., Drake S.A., Bastian S.A., 1992, ApJ, 393, 341

Lo K.K., Bray J.D., Hobbs G., et al., 2012, MNRAS, 421, 3316

Louarn P., Le Queau D., 1996a, P&SS, 44, 199

Louarn P., Le Queau D., 1996b, P&SS, 44, 211

Melrose D.B., Dulk G.A., 1982, ApJ, 259, 844

Menietti J.D., Mutel R.L., Christopher I.W., Hutchinson K.A., Sigwarth J.B, 2011, JGRA, 116, 12219

Mutel R.L., Christopher I.W., Pickett J.S., 2008, GeoRL, 35, 7104

Nichols J.D., Burleigh M.R., Casewell S.L., et al., 2012, ApJ, 760, 59

Oksala M.E., Wade G.A., Townsend R.H.D., et al., 2012, MNRAS, 419, 959

Ravi V., Hobbs G., Wickramasinghe D., Champion D.J., Keith M., 2010, MNRAS, 408, L99

Route M., Wolszczan A., 2012, ApJ, 747, L22

Route M., Wolszczan A., 2013, ApJ, 773, 18

Stevens I.R., George S.J., 2010, ASPC, 422, 135

Stift, M.J., 1973, A&A, 22,209

Speir D.C., et al., 2014, PRL, 113, 155002

Trigilio C., Leto P., Leone F., Umana G., Buemi C., 2000, A&A, 362, 281

Trigilio C., Leto P., Umana G., Leone F., Buemi C.S., 2004, A&A, 418, 593

Trigilio C., Leto P., Umana G., Buemi C.S., Leone F., 2008, MNRAS, 384, 1437

Trigilio C., Leto P., Umana G., Buemi C.S., Leone F., 2011, ApJ, 739, L10

Williams P.K.G., Berger, E., Irwin J., et al., 2015, ApJ, 799, 192

Wu C.S., Lee L.C. 1979, ApJ, 230, 621

Zarka, P, 1998, JGR, 103, 20159